Dalton Transactions

ROYAL SOCIETY OF CHEMISTRY

COMMUNICATION

View Article Online
View Journal | View Issue

Cite this: *Dalton Trans.*, 2021, **50**, 11365

Received 7th June 2021,
Accepted 22nd July 2021

DOI: 10.1039/d1dt01861b

rsc.li/dalton

A hybrid zeolitic imidazolate framework-derived $ZnO/ZnMoO_4$ heterostructure for electrochemical hydrogen production†

Yang Li, [a] Shumei Chen,*[a] Xin Wu, [b] Huabin Zhang *[c] and Jian Zhang [b]

Sustainable hydrogen fuel supply through electrochemical water splitting requires highly efficient, low-cost and robust electrocatalysts. Interface engineering is of key importance to improve the catalytic performance in a heterogeneous electrocatalytic system. Herein, a porous microcubic framework composed of a ZnO/$ZnMoO_4$ heterostructure (ZnO@$ZnMoO_4$) is prepared by a hybrid zeolitic imidazolate framework-derived oxidation method, and it shows much enhanced hydrogen evolution reaction (HER) activity in alkaline media. The overpotential (at 10 mA cm^{-2}) for ZnO@$ZnMoO_4$ is significantly reduced by 30% and 20% compared with those for virgin ZnO (v-ZnO) and polycrystalline zinc molybdenum oxide (PZMO), respectively. The enhanced electrocatalytic activity should be attributed to the ZnO/$ZnMoO_4$ heterostructure, which can synergistically facilitate the charge transport. This work provides a more structured design strategy for electrocatalysts for future electrochemical energy conversion systems.

Electrocatalytic water splitting into hydrogen (H_2) is a promising alternative to realize renewable energy supply and mitigate environmental issues.[1,2] Currently, Pt and Pt-based alloys are recognized as the state-of-the-art electrocatalysts for the hydrogen evolution reaction (HER).[3,4] However, the high price and scarcity hamper their widespread utilization. Therefore, it is urgent to develop low-cost and exceptionally effective catalysts to replace Pt and Pt-based electrocatalysts. As an earth-abundant transition metal, molybdenum (Mo)-based compounds, such as sulfides,[5,6] carbides,[7] nitrides,[8,9] phosphides,[10] selenides[11] and oxides,[12,13] have exhibited Pt-like catalytic activity for the HER. Particularly, Mo-based bimetallic compounds show richer redox sites compared with their Mo-based monometallic counterparts, hence a significant enhancement of the electrochemical performance is observed.[14] For instance, Tran *et al.* have reported that Cu_2MoS_4 shows higher HER activity over a wide pH range than MoS_2.[15] Xiong *et al.* have synthesized Co covalently doped MoS_2 (Co-MoS_2) and used it as an effective electrocatalyst for alkaline water splitting.[16] Despite the great achievements, limited work is available on Mo-based bimetallic oxide (MBO) electrocatalysts for the HER.

The low intrinsic conductivity of MBO electrocatalysts limits their widespread use.[17] Construction of heterostructured electrocatalysts can serve as an efficacious approach to achieve high performance in the electrocatalytic HER.[18–20] Compared with a single catalyst, heterostructured electrocatalysts could show a combination of the strengths of their parent phases.[21,22] Moreover, the built-in electric fields or chemical potential differences at the heterostructure can provide a driving force for charge transfer.[23–25] Co-aggregation and epitaxial growth are two common methods for the preparation of heterostructured electrocatalysts, but tend to lower their accessible active surface area.[26] Therefore, it is crucial to explore new methods for realizing the nano-sized heterostructure of MBO electrocatalysts.

Metal–organic frameworks (MOFs) have emerged as an interesting class of functional materials and precursors of inorganic materials for electrochemical energy-related applications.[27–30] As a subfamily of MOFs, Zn, Mo-based hybrid zeolitic imidazolate frameworks (HZIF-Zn/Mo) with excellent stability and porous structures demonstrate great potential in the electrocatalytic field.[31–33] The atomic-level structural uniformity of HZIFs can realize the intergrowth of different functional materials at the molecular level under desired conditions, resulting in the construction of a Mo-based heterostructured catalyst in a flexible and controllable manner.[34] Zhang *et al.* have constructed an ultrasmall MoC/MoS_2 heterostructure using HZIFs as the precursor and the obtained $MoCS_x$ heterostructure exhibits much enhanced oxygen reduction activity.[35] In this regard, the HZIF-assisted

[a]*College of Chemistry, Fuzhou University, Fuzhou 350108, China. E-mail: csm@fzu.edu.cn*
[b]*State Key Laboratory of Structural Chemistry, Fujian Institute of Research on the Structure of Matter, Chinese Academy of Sciences, Fuzhou, 350002, China*
[c]*KAUST Catalysis Center (KCC), Physical Sciences and Engineering Division, King Abdullah Uniersity of Science and Technology (KAUST), Thuwal 23955-6900, Saudi Arabia. E-mail: Huabin.Zhang@kaust.edu.sa*

†Electronic supplementary information (ESI) available: Experimental details, CV, and C_{dl} plots. See DOI: 10.1039/d1dt01861b

strategy can be an economical strategy for preparing heterostructured MBO electrocatalysts.

Herein, we prepared $ZnO@ZnMoO_4$ *via* direct oxidation of HZIFs and systematically evaluated its HER performance in an alkaline medium. The obtained $ZnO@ZnMoO_4$ integrates the structural advantages of different functional subunits. Specifically, the variable oxidation states of the elements in $ZnMoO_4$ ensure more active sites for the HER. The electrical coupling at the $ZnO/ZnMoO_4$ heterostructure is beneficial for electron transfer and structural stability. Moreover, benefiting from the mutual promoted action at the interface by the synergistic effect of two components, reconstructed active centers with higher intrinsic activity are established. Impressively, the obtained $ZnO@ZnMoO_4$ hybrid exhibits much boosted HER activity in alkaline media.

Post-annealing of the performed HZIF-Zn/Mo under air results in the formation of $ZnO@ZnMoO_4$. In this process, the organic moieties in HZIF-Zn/Mo are evaporated at a high temperature, whereas the Zn and Mo components react with O to form ZnO and $ZnMoO_4$. The X-ray diffraction (XRD) spectrum shows the coexistence of ZnO and $ZnMoO_4$ in $ZnO@ZnMoO_4$ (Fig. S1†).[36] Scanning electron microscopy (SEM) and transmission electron microscopy (TEM) images show that the obtained $ZnO@ZnMoO_4$ retains the original cubic shape from the parent HZIF-Zn/Mo and exhibits a rougher surface (Fig. 1a–e and S2†). A closer observation of the cracked particle reveals that the interior of $ZnO@ZnMoO_4$ is composed of numerous loosely assembled nanoparticles (Fig. 1b and c). The formation of the loose structure probably originates from the consumption of the organic moiety in the pyrolysis process. The high-resolution TEM (HRTEM) image shows clear lattice fringes with lattice spacings of 0.28 and 0.23 nm, corresponding to the (100) and (130) crystal planes of ZnO and $ZnMoO_4$, respectively, revealing the formation of an intimate $ZnO/ZnMoO_4$ heterostructure (Fig. 1f).[37,38] Energy-dispersive X-ray spectroscopy (EDS) investigation confirms that $ZnO@ZnMoO_4$ is composed of Zn, Mo and O (Fig. S3†). High-angle annular dark-field scanning transmission electron microscopy (HAADF-STEM) coupled with elemental mapping images show the homogeneous distribution of O, Zn and Mo in the $ZnO@ZnMoO_4$ framework (Fig. 1g–i). Virgin ZnO (v-ZnO) was fabricated by performing a similar synthetic process with $ZnO@ZnMoO_4$ except for using ZIF-8 as the precursor and polycrystalline zinc molybdenum oxide (PZMO) was also prepared and they were used as the references (Figs. S4 and S5†).

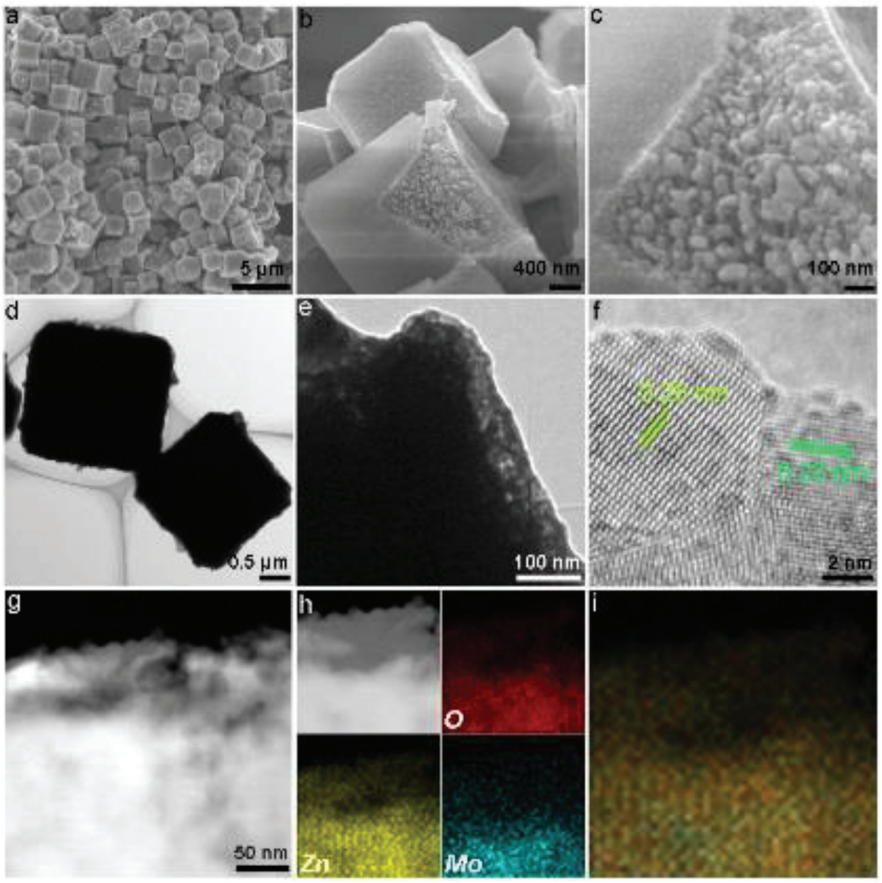

Fig. 1 (a–c) SEM images of $ZnO@ZnMoO_4$. (d and e) TEM images of $ZnO@ZnMoO_4$. (f) HRTEM image of $ZnO@ZnMoO_4$. (g–i) HAADF-STEM and elemental mapping images of $ZnO@ZnMoO_4$.

The surface chemical state of $ZnO@ZnMoO_4$ is investigated by X-ray photoelectron spectroscopy (XPS). Compared with v-ZnO, additional Mo 3d, Mo $3p_{3/2}$ and Mo $3p_{1/2}$ profiles are observed for $ZnO@ZnMoO_4$, suggesting the co-existence of Zn, Mo and O (Fig. 2a). The O 1s spectrum can be well divided into three peaks (Fig. 2b). The peaks at 529.8 and 530.8 eV correspond to the Mo–O and Zn–O bonds, respectively.[39] The higher energy peak at 532 eV is ascribed to chemisorbed oxygen.[40–42] In Fig. 2c, the Zn $2p_{3/2}$ and Zn $2p_{1/2}$ peaks shift toward the higher binding energy after $ZnMoO_4$ modification, indicating the interaction of ZnO and $ZnMoO_4$.[43] In the high-resolution Mo 3d spectrum, the doublet located at the higher binding energy is attributed to the Mo^{6+} species, while the doublet with the lower binding energy originates from $Mo^{\delta+}$ ($\delta < 6$) (Fig. 2d).[44] The appearance of $Mo^{\delta+}$ could be due to the electronic redistribution at the $ZnO/ZnMoO_4$ nanointerface *via* charge transfer, strongly suggesting the chemical binding of the *in situ* formed ZnO and $ZnMoO_4$.[45] The structural information of $ZnO@ZnMoO_4$ is further analyzed using the Raman spectrum (RM). The E_{2L}-E_{2H} mode at 332 cm^{-1} signifies the second order non-polar scattering arising from the ZnO zone boundary centre (Fig. 2e).[46] The peak at 437 cm^{-1} is the E_2(high) mode of ZnO owing to the vibration of the oxygen atom, indicating the high crystal quality of ZnO. The disappearance of E_2(high) for $ZnO@ZnMoO_4$ demonstrates the decreased *c*-axis growth and worse crystallization of the ZnO component, which could be attributed to the chemical bonding of ZnO with $ZnMoO_4$ because of their intergrowth during the annealing process.[47] The E_1(LO) mode observed at 583 cm^{-1} means the existence of the oxygen vacancy and Zn interstitial in both v-ZnO and $ZnO@ZnMoO_4$. The N_2 adsorption and desorption isotherms show that the Brunauer–Emmett–Teller (BET) surface area of $ZnO@ZnMoO_4$ is 19.6 m^2 g^{-1}, higher than that of v-ZnO (15.5 m^2 g^{-1}) (Fig. 2f).

The HER activities of the as-prepared catalysts are investigated in 1.0 M KOH. Fig. 3a shows the linear sweep voltammetry (LSV) curves of different electrode materials. Unsurprisingly, a commercial Pt/C (20 wt%) catalyst demonstrates the best HER activity, showing near ~0 V onset potential. v-ZnO exhibits inferior HER activity, requiring an overpotential (η_{10}) of 0.52 V at a current density of 10 mA cm^{-2}. A positively shifted η_{10} is observed for PZMO (0.45 V), indicating that more active sites existed in the constructed bimetallic oxide. The HER activity is further accelerated by the $ZnO@ZnMoO_4$ catalyst, the η_{10} value of which is reduced to 0.36 V, 30%, 20% and 18% lower than those of v-ZnO, PZMO and their mechanical mixture (ZnO/PZMO), respectively. These results indicate that the interface optimizing between ZnO and $ZnMoO_4$ can induce a synergistically enhanced HER activity.

The alkaline water-splitting kinetics of various catalysts is revealed by Tafel plots derived from the polarization curves. The Tafel slope of $ZnO@ZnMoO_4$ is confirmed to be 63 mV dec^{-1} and smaller than those of PZMO (85 mV dec^{-1}), v-ZnO (479 mV dec^{-1}) and ZnO/PZMO (72 mV dec^{-1}), indicating the

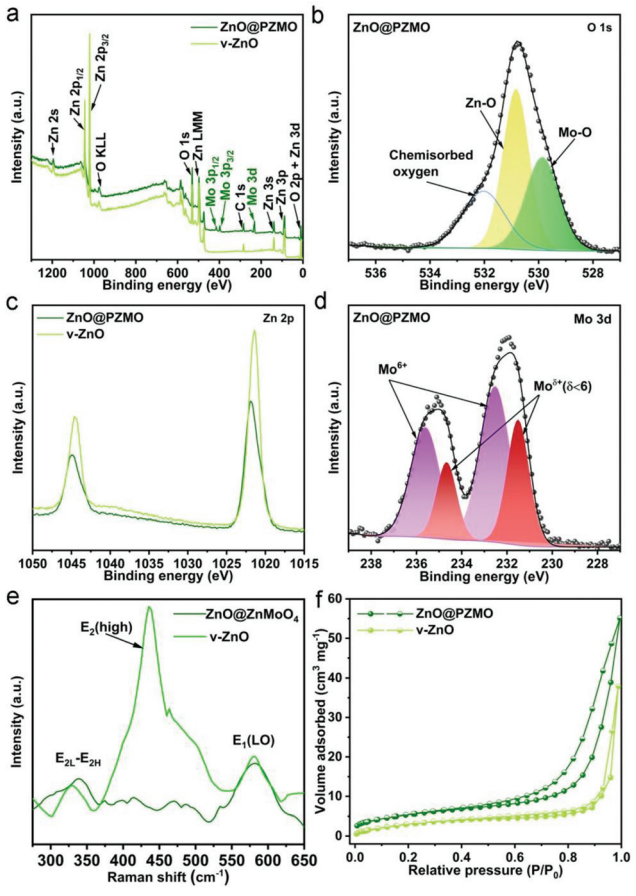

Fig. 2 (a) XPS survey spectra of $ZnO@ZnMoO_4$ and v-ZnO. The high resolution of (b) O 1s, (c) Zn 2p, and (d) Mo 3d of $ZnO@ZnMoO_4$ and v-ZnO, respectively. (e) Raman spectra and (f) N_2 adsorption–desorption isotherms of $ZnO@ZnMoO_4$ and v-ZnO.

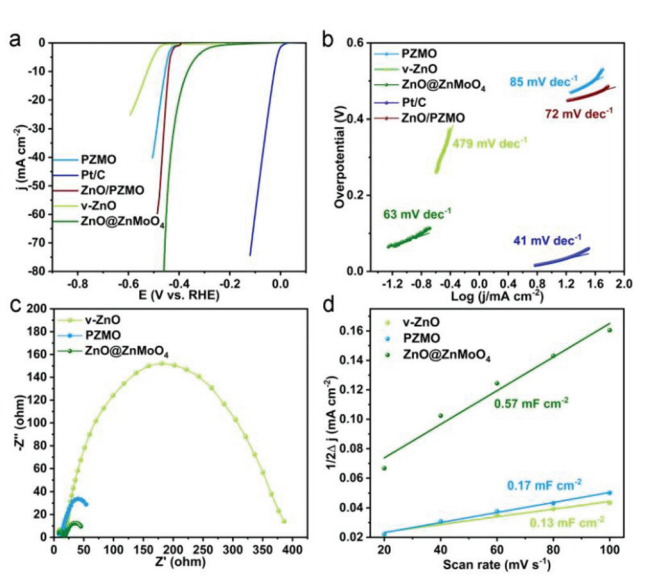

Fig. 3 (a–c) LSV curves, Tafel plots and EIS of various electrodes in 1.0 M KOH. (d) The capacitive currents as a function of scan rate for various electrodes.

higher HER rate of ZnO@$ZnMoO_4$ (Fig. 3b). This result suggests that the HER over ZnO@$ZnMoO_4$ proceeds *via* a Heyrovsky-dominated Volmer–Heyrovsky mechanism, which indicates that the sluggish dissociation of H_2O is the rate determining step.[48,49] The electrode kinetics of ZnO@$ZnMoO_4$ in the HER process is evaluated by electrochemical impedance spectroscopy (EIS). The semicircle in the low-frequency range on the Nyquist plot derives the charge-transfer resistance (R_{ct}), which is highly related to the electrocatalytic kinetics. The EIS results show that ZnO@$ZnMoO_4$ has a smaller R_{ct} value than the other samples, indicating a faster charge transfer rate at the ZnO@$ZnMoO_4$/electrolyte interface (Fig. 3c).

The boosted HER activity of ZnO@$ZnMoO_4$ could originate from the high electrochemically active surface area (ECSA). To confirm this point, we investigate the double-layer capacitance (C_{dl}) which is positively proportional to the ECSA by performing cyclic voltammetry (CV) measurements. The current response in the CV test is ascribed to the exposed surface area of the electrode in the electrolyte. As shown in Fig. S6,† the highest C_{dl} value of ZnO@$ZnMoO_4$ indicates the most electrolyte-accessible surface area, which could originate from its interior porous structure. The chronoamperometric response at a fixed potential of −0.4 V is measured to investigate the stability of ZnO@$ZnMoO_4$ (Fig. S7†). During the testing, the minor fluctuations indicate the hydrogen gas generation, accumulation and desorption. A less than 20% degradation of the initial current after 40 000 s is observed, demonstrating the strong durability of ZnO@$ZnMoO_4$. The XRD, HRTEM and EDS characterization of ZnO@$ZnMoO_4$ after the HER reveals the decreased crystallinity of the $ZnMoO_4$ moiety, which may result from the etch in the alkaline medium during the HER process.

In summary, in this work we developed an effective strategy to accelerate the water-splitting activity of $ZnMoO_4$ by cooperating with ZnO to form an interfacial heterostructure. The experimental results demonstrate that the boosted HER activity derives from the modulated electronic states at the heterointerface, which offer abundant active sites and improve the conductivity of $ZnMoO_4$. Profiting from the aforementioned point, ZnO@$ZnMoO_4$ shows a low onset overpotential, small Tafel slope and good cycling stability. This work not only develops a low-cost and efficient HER electrocatalyst, but also delivers a HZIF-derived method, which could be extended to the synthesis of other multifunctional Mo-based catalysts for energy conversion and storage applications.

Conflicts of interest

There are no conflicts to declare.

Acknowledgements

This work was supported by NSFC (21871050, 21773242).

Notes and references

1 S. Chu and A. Majumdar, *Nature*, 2012, **488**, 294–303.
2 D. Deng, K. S. Novoselov, Q. Fu, N. Zheng, Z. Tian and X. Bao, *Nat. Nanotechnol.*, 2016, **11**, 218–230.
3 H. Zhang, P. An, W. Zhou, B. Y. Guan, P. Zhang, J. Dong and X. W. D. Lou, *Sci. Adv.*, 2018, **4**, 6657.
4 H. Zhang, X. F. Lu, Z. P. Wu and X. W. D. Lou, *ACS Cent. Sci.*, 2020, **6**, 1288–1301.
5 H. Zhang, L. Yu, T. Chen, W. Zhou and X. W. D. Lou, *Adv. Funct. Mater.*, 2018, **28**, 1807086.
6 Y. Li, S. Zuo, Q. H. Li, X. Wu, J. Zhang and J. Zhang, *Nano Lett.*, 2021, **21**, 1848–1855.
7 H. Zhang, Z. Ma, G. Liu, L. Shi, J. Tang, H. Pang, K. Wu, T. Takei, J. Zhang, Y. Yamauchi and J. Ye, *NPG Asia Mater.*, 2016, **8**, e293.
8 Y. Zhu, G. Chen, X. Xu, G. Yang, M. Liu and Z. Shao, *ACS Catal.*, 2017, **7**, 3540–3547.
9 H. Jin, X. Liu, A. Vasileff, Y. Jiao, Y. Zhao, Y. Zheng and S. Z. Qiao, *ACS Nano*, 2018, **12**, 12761–12769.
10 J. S. Li, S. Zhang, J. Q. Sha, H. Wang, M. Z. Liu, L. X. Kong and G. D. Liu, *ACS Appl. Mater. Interfaces*, 2018, **10**, 17140–17146.
11 D. Gao, B. Xia, C. Zhu, Y. Du, P. Xi, D. Xue, J. Ding and J. Wang, *J. Mater. Chem. A*, 2018, **6**, 510–515.
12 L. Wu, X. Wang, Y. Sun, Y. Liu and J. Li, *Nanoscale*, 2015, **7**, 7040–7044.
13 J. Ahmed, M. A. Majeed Khan and S. M. Alshehri, *Mater. Lett.*, 2021, **284**, 128996.
14 X. Y. Yu and X. W. David Lou, *Adv. Energy Mater.*, 2018, **8**, 1701592.
15 P. D. Tran, M. Nguyen, S. S. Pramana, A. Bhattacharjee, S. Y. Chiam, J. Fize, M. J. Field, V. Artero, L. H. Wong, J. Loo and J. Barber, *Energy Environ. Sci.*, 2012, **5**, 8912.
16 Q. Xiong, Y. Wang, P. F. Liu, L. R. Zheng, G. Wang, H. G. Yang, P. K. Wong, H. Zhang and H. Zhao, *Adv. Mater.*, 2018, **30**, 1801450.
17 F. Han, S. Yun, J. Shi, Y. Zhang, Y. Si, C. Wang, N. Zafar, J. Li and X. Qiao, *Appl. Catal., B*, 2020, **273**, 119004.
18 H. Zhang, Z. Ma, J. Duan, H. Liu, G. Liu, T. Wang, K. Chang, M. Li, L. Shi, X. Meng, K. Wu and J. Ye, *ACS Nano*, 2016, **10**, 684–694.
19 H. Zhang, W. Cheng, D. Luan and X. W. D. Lou, *Angew. Chem., Int. Ed.*, 2021, **60**, 2–22.
20 H. Zhang, P. Zhang, M. Qiu, J. Dong, Y. Zhang and X. W. D. Lou, *Adv. Mater.*, 2019, **31**, 1804883.
21 G. Xu, H. Zhang, J. Wei, H. X. Zhang, X. Wu, Y. Li, C. Li, J. Zhang and J. Ye, *ACS Nano*, 2018, **12**, 5333–5340.
22 X. Wu, S. Zuo, M. Qiu, Y. Li, Y. Zhang, P. An, J. Zhang, H. Zhang and J. Zhang, *Chem. Eng. J.*, 2021, **420**, 127681.
23 C. Long, X. Li, J. Guo, Y. Shi, S. Liu and Z. Tang, *Small Methods*, 2018, **3**, 1800369.
24 L. Zheng, F. Teng, X. Ye, H. Zheng and X. Fang, *Adv. Energy Mater.*, 2019, **10**, 1902355.
25 X. Wu, J. Dong, M. Qiu, J. Kong, Y. Zhang, Y. Li, G. Xu, J. Zhang and J. Ye, *Nano Energy*, 2018, **45**, 109–117.

26 X. Lu, J. Pan, E. Lovell, T. H. Tan, Y. H. Ng and R. Amal, *Energy Environ. Sci.*, 2018, **11**, 1898–1910.
27 J. Li, Z. Meng, D. J. L. Brett, P. R. Shearing, N. T. Skipper, I. P. Parkin and S. Gadipelli, *ACS Appl. Mater. Interfaces*, 2020, **12**, 42696–42703.
28 S. Gadipelli, Z. Li, Y. Lu, J. Li, J. Guo, N. T. Skipper, P. R. Shearing and D. J. L. Brett, *Adv. Sci.*, 2019, **6**, 1901517.
29 Y. Qin, X. Han, S. Gadipelli, J. Guo, S. Wu, L. Kang, J. Callison and Z. Guo, *J. Mater. Chem. A*, 2019, **7**, 6543–6551.
30 C. Leng, Z. Zhao, Y. Song, L. Sun, Z. Fan, Y. Yang, X. Liu, X. Wang and J. Qiu, *Nano-Micro Lett.*, 2021, **13**, 132.
31 Y. Li, X. Wu and J. Zhang, *Nanoscale*, 2019, **11**, 15763–15769.
32 Y. Li, R. Zhang, W. Zhou, X. Wu and J. Zhang, *ACS Nano*, 2019, **13**, 5533–5540.
33 Y. Li, X. Wu and J. Zhang, *ACS Appl. Energy Mater.*, 2018, **1**, 3377–3384.
34 Y. T. Xu, Z. M. Ye, J. W. Ye, L. M. Cao, R. K. Huang, J. X. Wu, D. D. Zhou, X. F. Zhang, C. T. He, J. P. Zhang and X. M. Chen, *Angew. Chem. Int. Ed*, 2019, **58**, 139–143.
35 Y. Li, S. Zuo, X. Wu, Q. Li, J. Zhang and J. Zhang, *Small*, 2021, **17**, 2003256.
36 D. Wang, G. Du, D. Han, Q. Su, M. Zhang, S. Ding and B. Xu, *J. Alloys Compd.*, 2021, **859**, 157792.
37 Y. G. Lin, Y. K. Hsu, Y. C. Chen, L. C. Chen, S. Y. Chen and K. H. Chen, *Nanoscale*, 2012, **4**, 6515–6519.
38 K. Zhang, J. He, R. Shen, X. Sun, Q. Ouyang, Y. Chen, Y. Gao and W. Ji, *Opt. Mater.*, 2020, **99**, 109570.
39 X. Yang, H. Wang, W. Dou, P. Wang, X. Yang, X. Pan, B. Lu and H. Mao, *Phys. Chem. Chem. Phys.*, 2020, **22**, 2399–2404.
40 X. Zhao, J. Feng, J. Liu, J. Lu, W. Shi, G. Yang, G. Wang, P. Feng and P. Cheng, *Adv. Sci.*, 2018, **5**, 1700590.
41 H. Zhang, W. Zhou, J. Dong, X. F. Lu and X. W. Lou, *Energy Environ. Sci.*, 2019, **12**, 3348–3355.
42 X. Wu, H. Zhang, S. Zuo, J. Dong, Y. Li, J. Zhang and Y. Han, *Nano-Micro Lett.*, 2021, **13**, 136.
43 L. Meng, X. Yang, H. Chai, Z. Lv and T. Yang, *ACS Appl. Mater. Interfaces*, 2019, **11**, 26491–26499.
44 L. Li, Z. Qin, L. Ries, S. Hong, T. Michel, J. Yang, C. Salameh, M. Bechelany, P. Miele, D. Kaplan, M. Chhowalla and D. Voiry, *ACS Nano*, 2019, **13**, 6824–6834.
45 X. Wu, J. Dong, M. Qiu, Y. Li, Y. Zhang, H. Zhang and J. Zhang, *Nanoscale Horiz.*, 2020, **5**, 359–365.
46 T. Marimuthu, N. Anandhan and R. Thangamuthu, *Appl. Surf. Sci.*, 2018, **428**, 385–394.
47 H. Jiang, X. Zhang, W. Gu, X. Feng, L. Zhang and Y. Weng, *Chem. Phys. Lett.*, 2018, **711**, 100–106.
48 S. Ye, F. Luo, T. Xu, P. Zhang, H. Shi, S. Qin, J. Wu, C. He, X. Ouyang, Q. Zhang, J. Liu and X. Sun, *Nano Energy*, 2020, **68**, 104301.
49 H. Wang, X. Xiao, S. Liu, C. L. Chiang, X. Kuai, C. K. Peng, Y. C. Lin, X. Meng, J. Zhao, J. Choi, Y. G. Lin, J. M. Lee and L. Gao, *J. Am. Chem. Soc.*, 2019, **141**, 18578–18584.